Moon Orbiter "Izumi" for Lunar Water Exploration

Kentaro Taniguchi
Waseda University
3-4-1, Okubo, Shinjuku, Tokyo, Japan
t.kentaro@ruri.waseda.jp

Miwa Tsurumi
Aoyama Gakuin University
5-10-1, Fuchinobe, Sagamihara, Kanagawa, Japan

Ryusei Komatsu
The Graduate University for Advanced Studies, SOKENDAI
3-1-1 Yoshinodai, Sagamihara, Kanagawa, Japan

Faculty Advisor: Teruaki Enoto
RIKEN / Kyoto University

ABSTRACT

NASA's Artemis program focuses on the water resources on the Moon. As lunar exploration probes with high spatial resolutions can identify potential drilling points on the lunar surface, this study proposes a mission that focuses on neutrons generated by galactic cosmic rays that leak into space and contain information regarding the amount of water within the lunar subsurface. Neutron detectors used in previous lunar exploration mission probes have encountered challenges in achieving both high spatial resolution and statistical reliability. To overcome these challenges, the proposed mission satellite is equipped with the world's first imager proposed for thermal neutrons. The satellite aims to achieve the highest spatial resolution of 5 km and provide results with sufficient statistical reliability using lightweight optics. Furthermore, the satellite measures the lifetime of neutrons, and the results are compared with those obtained using two established methods on the ground. To accomplish these tasks, a 50-kg lunar orbiter is conceptually designed after several design iterations, including detailed simulations of the subsystems. The satellite observes water distribution from a lunar polar frozen orbit over a one-year mission period.

MAIN MISSION INTRODUCTION

The Artemis mission aims to build a manned base on the Moon, as a pivotal point, for deep-space human exploration beyond the Moon. The presence of water resources on the Moon is an important factor that facilitates this mission, as water can be utilized to produce rocket propellants and sustain human life.

Neutrons and electromagnetic waves (near-infrared (NIR)/infrared (IR) and synthetic aperture radar (SAR)) are mainly used to observe lunar water resources. Neutron surveys are particularly important for identifying underground water resources. As illustrated in Figure 1, the NIR and IR surveys have detected water near the surface [1], whereas neutron and SAR surveys have detected water within shallow subsurfaces. Although SAR surveys require prior knowledge of the subsurface layering, neutron surveys can directly detect hydrogen, a constituent of water.

Studies have reported that water is stored in permanent shadows inside the polar craters [2]. The Shackleton crater, a typical crater in the lunar South Pole region, is a potential storage site. Kaguya revealed that its diameter is approximately 20 km, and the permanently shadowed region (PSR) at the bottom of the crater has a diameter of approximately 6.6 km [3]. Therefore, an observation method with a spatial resolution of approximately 5 km is required to detect the presence of water in the PSR of the crater or in the regions with the same size. While electromagnetic surveys featured a spatial resolution of less than a few hundred meters [1], neutron surveys featured a spatial resolution of 50 km in the first exploration and 10 km [4] in the most recent exploration, indicating the inherent difficulties in conducting neutron surveys.

High spatial resolution has not been achieved in neutron surveys because existing methods do not allow for good spatial resolution along with a sufficient number of detections to provide accurate statistics. The first neutron detector operating in the lunar orbit was aboard the Lunar Prospector (LP) spacecraft launched by NASA in 1998. The detector could not distinguish between the arrival directions of incoming neutrons and the detected neutrons arriving from all the directions. Consequently,

the spatial resolution was 45 km at an altitude of 30 km [2]. The LunarH-Map, launched in 2022, is attempting to reach a lower altitude of 15 km with a spatial resolution of 15 km [5], which is still insufficient to reach the target resolution of 5 km.

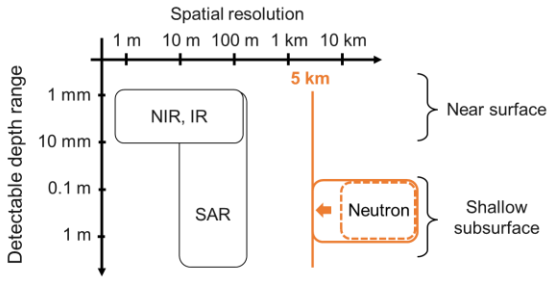

Figure 1: Detectable depth range and spatial resolution of different observation methods [1]

Another approach is to reduce the field of view (FOV). The lunar exploration neutron detector (LEND) aboard the Lunar Reconnaissance Orbiter, launched in 2009, incorporated this method and achieved a spatial resolution of 10 km from an altitude of 50 km [4]. However, the shielding material used to achieve a narrower FOV eliminates the neutrons outside the FOV; consequently, the number of neutrons entering the detector is insufficient, which in turn diminishes the statistical validity.

Based on the previous explorations, it is evident that the two existing methods, i.e., narrowing the FOV and lowering the altitude summarized in Figure 2, cannot realistically achieve a resolution less than 10 km, the best achieved by LEND. Therefore, this study proposes a neutron telescope for detecting the arrival directions of thermal neutrons within the FOV while maintaining a sufficiently wide FOV to ensure statistical validity of the results. A statistically significant number of detections can be obtained for observations made with a spatial resolution of 5 km.

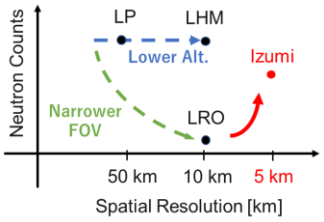

Figure 2: Neutron count vs. spatial resolution achieved by previous missions incorporating the two existing methods and the proposed mission, showcasing its novelty

MAIN MISSION ANALYSIS-NEUTRON LEAKAGE AND PROPAGATION

The presence of water resources can be determined by detecting the neutron leakage from the lunar surface. As shown in Figure 3, neutrons are generated in the lunar surface layer as a product of the reaction between the galactic cosmic rays (GCRs) bombarding the lunar surface and the soil. If present, hydrogen atoms of nearly equal masses moderate neutrons with elastic scattering, which ends up with neutron leaking from the surface with reduced energy. Therefore, observing the spatial fluctuation of the neutron flux makes it possible to estimate the number of hydrogen atoms that contribute to the deceleration of neutrons. The amount of water can be estimated by assuming that all the detected hydrogen is in the form of water.

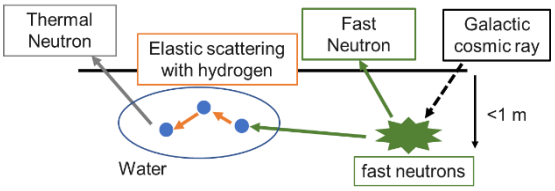

Figure 3: Neutron generation process. Generated neutron moderates through elastic scattering with hydrogen in water

First, neutron fluxes observed by a satellite in orbit were calculated through a simulation of neutron leakage from the surface layer through Geant4 analysis [6]. As shown in Figure 4, the analysis revealed that the energy spectrum of the flux varied with different hydrogen densities, as the thermal neutron flux increased with increasing hydrogen density. The increase or decrease in flux with hydrogen density can be expressed in terms of the hydrogen density by expressing the flux relative to the hydrogen-free soil. Using the above relationship, in actual observations, the hydrogen density can be estimated from the flux variations. Note that 100 and 500 ppm hydrogen correspond to approximately 0.1 and 0.5 wt.% of water, respectively.

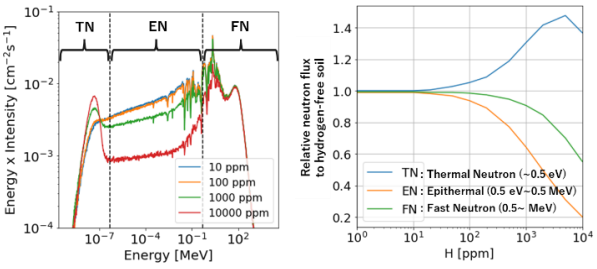

Figure 4: (Left) Energy spectrum of leakage neutrons (Right) Relative neutron flux to hydrogen-free soil [6]

Considering the orbital propagation of neutrons [7], the flux at a given energy is determined such that the satellite can make observations from each direction at a given altitude. This calculation assumed a spherically symmetric moon. First, based on two parameters—the velocity observed from the satellite and the direction of flight at the zenith angle—the flight trajectory was determined through orbital mechanics, as indicated by the red dotted line in Figure 5. Next, the flux on the lunar surface determined from orbit was calculated using the leakage flux on the lunar surface obtained from the leakage analysis, assuming that the neutron density only decreases owing to the exponential decay of neutrons. To investigate the dependency on hydrogen, fluxes on soils with different hydrogen densities were used, which provided relative flux data, as shown in Figure 4.

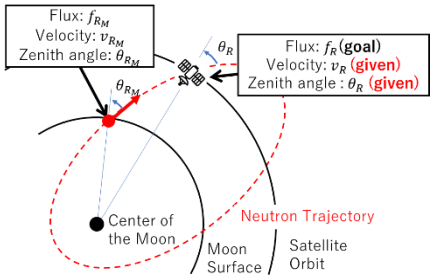

Figure 5: Model of a neutron propagating to orbit

For example, the angular profiles of the neutron flux at a height of 20 km are shown in Figure 6. Here, the energy was divided into thermal neutron (TN), epithermal neutron (EN), and fast neutron (FN) regions. As shown in Figure 6, in all the energy bands, the flux from the nadir direction was the largest. The expected neutron count can be estimated by integrating the directional flux over a detector FOV with the detector efficiency.

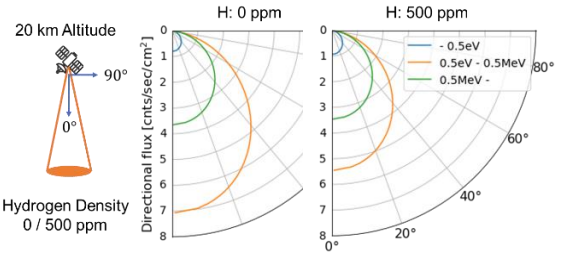

Figure 6: Directional neutron flux on orbit

MAIN MISSION REQUIREMENTS

The main mission had two observation targets. The first was the Shackleton crater located at approximately 90° south latitude. Figure 7 shows a map of the lunar South Pole and the names of its craters. The craters at the South Pole are not affected by lunar rotation; therefore, a satellite can observe them for a sufficient period. In the LEND mission, craters at 90° south were observed with a spatial resolution of 10 km. The proposed mission aims to achieve a better spatial resolution of 5 km and detect 100-ppm difference in hydrogen density with ±3σ statistical reliability, which is equivalent to LEND's results [4].

The second observation targets were craters between 85° and 88° south latitudes. These craters are ideal for robotic exploration in terms of sunlight and communication, and there are several such ongoing missions. However, the target latitude range of 85° to 88° south latitude is challenging, because it is difficult to obtain sufficient observation time owing to the rotation of the Moon, and no statistically reliable high-resolution observation results have been obtained thus far. Therefore, to achieve a statistical reliability of ±3σ, the target spatial resolution was reduced to 10 km and the hydrogen density difference to detect was reduced to 500 ppm. These requirements are listed in Table 1.

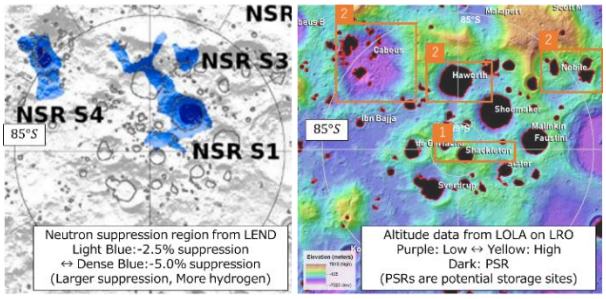

Figure 7: (Left) Potential water storage sites from LEND results [4] (Right) PSR regions with crater names from the altimeter on Lunar Reconnaissance Orbiter (LRO) [8]

Table 1: Main mission requirements

Reqt. 1	Map hydrogen density in the Antarctic region (88–90° south latitude) with a spatial resolution of 5 km and distinguished differences in density of 100 ppm with a statistical reliability of 3σ.
Reqt. 2	Map hydrogen density near the Antarctic region (85–88° south latitude) with a spatial resolution of 10 km and distinguished differences in density of 500 ppm with a statistical reliability of 3σ.

MAIN MISSION DETECTOR: NEUTRON TELESCOPE

To fulfill mission requirements, a thermal neutron imager, representing a significant breakthrough in the existing technology, is necessary. In this mission, we propose a pioneering concept: the world's first neutron telescope for remote sensing, capable of enhancing spatial resolution while maintaining the FOV. Additionally, the neutron mirror has potential other applications such as CT imaging and moisture meters for construction. A neutron telescope is composed of three components: a neutron reflector, optics, and a scintillation detector, as illustrated in Figure 8.

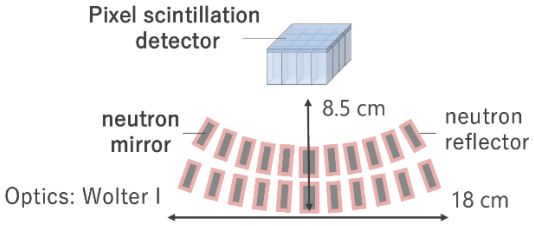

Figure 8: Schematics of a neutron telescope

Reflector of a neutron mirror

To reflect the neutrons, a neutron multilayer supermirror was used, and a schematic of a multilayer supermirror is shown in Figure 9. The fundamental principle of a multilayer supermirror is the "Bragg reflection." To achieve a high reflectivity, layers with decreasing intervals were stacked gradually, resulting in an increased energy range for reflection. In this mission, the neutron supermirror [9] developed by RIKEN/Kyoto University served as the neutron reflector. This technology comprises NiC/Ti multilayers deposited at varying layer intervals. The reflectance profile is shown in Figure 10, where the reflectivity is dependent on the neutron momentum transfer. Below the critical momentum transfer of 0.63 nm^{-1}, the reflectivity remains constant at 86%, The momentum transfer q can be expressed as follows:

$$q = \frac{4\pi \sin\theta}{\lambda}, \quad (1)$$

where λ and θ are the neutron wavelength and angle of incidence, respectively. The equation implies that neutrons with smaller incident angles and energies have smaller critical transfer momenta and higher reflectance.

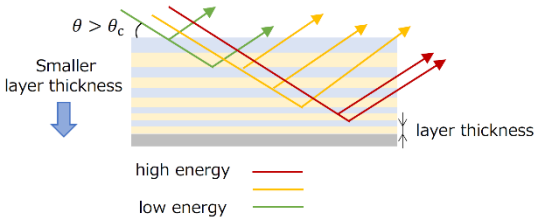

Figure 9: Schematic of a multilayer supermirror

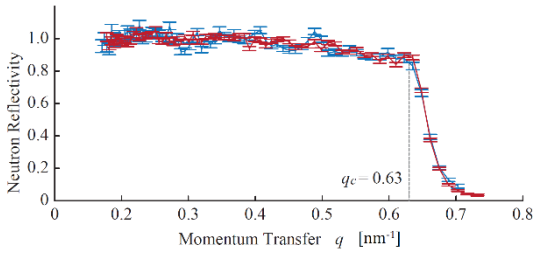

Figure 10: Reflectivity of neutron supermirror [9]

Optics of a neutron mirror

The neutron telescope was designed with Wolter I-type grazing incidence optics, which are widely employed in X-ray telescopes. The Wolter I-type can focus photons and neutrons at the focal point by reflecting them twice using two reflectors: a rotating parabolic mirror and a rotating hyperbolic mirror. The mirrors were manufactured using micromachine (MEMS) technology [10], which is under development at the Tokyo Metropolitan University for fabricating MEMS X-ray telescopes. A silicon substrate with microholes was smoothed, as it underwent plastic deformation at high temperatures. Subsequently, a NiC/Ti multilayer film can be deposited onto it, and finally, it can be formed into a Wolter I shape. The specifications of the neutron telescope are presented in Table 2.

Table 2: Specifications of the neutron telescope

Optic	Unit	Value
Energy	eV	<0.5
Field of view	deg	30
Angular resolution	deg	7.5
Focal length	mm	85
Diameter	mm	180
Effective area	cm^2	50
Detector	**Unit**	**Value**
Pixel size	cm x cm	1 x 1
Format	pix x pix	4 x 4
Area	cm^2	16

Integration of reflector and optics

The feasibility of neutron multilayer supermirror deposition onto the optics of a MEMS X-ray telescope is significant in realizing the world's first neutron telescope for remote sensing. The neutron multilayer supermirrors developed at the RIKEN/Kyoto University were produced through ion-beam sputtering deposition. However, it is generally difficult to deposit multilayer supermirrors on a microstructure, such as the optics of a MEMS X-ray telescope. Therefore, in such cases, atomic layer deposition (ALD) method can be used to facilitate the deposition process. This method can control the thickness of the layer at the atomic level, making it possible to deposit ultrathin layers on microstructures. ALD-processed surfaces can reflect even the undesirable surface roughness of the substrate. Because neutron reflectivity depends on the smoothness of the mirror, it is necessary to smoothen the surface of the silicon substrate before deposition to maintain high reflectivity. This was achieved by increasing the annealing time during the smoothing process in the optics manufacturing process. Therefore, it is possible to manufacture a neutron telescope by depositing NiC/Ti

multilayer supermirrors on the optics of a MEMS X-ray telescope.

Pixel scintillation detector

To detect the reflected neutrons from the telescope, a scintillator detector with a detection surface size of 4 cm × 4 cm was positioned at the focal plane, and the surface was then divided into pixels. The detector surface was covered with 16 GS20 glass scintillators, each measuring 1 cm × 1 cm × 2 cm in thickness and arranged in a 4 × 4 configuration. Additionally, to discriminate the background GCRs using the anti-simultaneous coefficient method, a single plastic scintillator EJ270 (ELJEN TECHNOLOGY) measuring 4 cm × 4 cm × 5 mm in thickness was placed at the top. To acquire the signal, an MPPC photodetector (Hamamatsu Photonics K.K.) was attached to the scintillators.

Fulfillment of main mission requirements

To evaluate whether the designed detector satisfied the mission requirements listed in Table 2, the following evaluation was conducted: To achieve a statistical accuracy of 3σ when observing the fluctuation rate δ, the difference to be observed must be greater than the statistical fluctuation. Based on these conditions, the number of neutrons required to satisfy the mission requirements can be calculated as follows [4]:

$$\delta N_{signal} > 3\sqrt{N_{total}} = 3\sqrt{N_{signal}}\sqrt{1+k},$$

$$\boldsymbol{N_{signal} = F\varepsilon S_{det} t_{obs} > \frac{X^2}{\delta^2}(1+k)}, \quad (2)$$

where N_{total} represents the number of neutrons detected by the detector; $X\sigma$ represents the statistical reliability (3σ); δ represents the detection variation rate (0.2); k represents the ratio of the background to the neutron counts to be detected ($k = N_{bgd}/N_{signal} = 3.65$); F represents the neutron flux (0.0465 $counts/s/cm^2$); ε represents the detection efficiency (0.95); S_{det} represents the effective detector area (204 cm^2); and t_{obs} represents the observation time (243 s)) of a target location on the Moon with a resolution of 10 km calculated by STK.

Transforming Equation (2) makes it possible to express the mission and detector parameters on the right and left sides, respectively, as demonstrated in Equation (3). The mission parameter was calculated to be 20 based on the given mission requirements; furthermore, from the aforementioned detector design, the detector parameter was calculated to be 41.7. Therefore, the designed detector satisfies the mission requirements.

$$\boldsymbol{\frac{\varepsilon S_{det}}{1+k} = 41.7 > 20 = \frac{X^2}{\delta^2}\frac{1}{F t_{obs}}} \quad (3)$$

SECOND MISSION INTRODUCTION

Neutron lifetime can be measured by detecting the neutrons in the lunar orbit simultaneously with the water exploration mission to effectively utilize the mission potential. Two established ground-based experimental methods, beam and bottle methods, have measured neutron lifetime as 888.0 ± 2.0 s and 879.4 ± 0.6 s, respectively [11]. However, the reason for the systematic error of 8.6 s between the measurements has not yet been determined. Therefore, a third measurement method that uses neutrons leaked from celestial bodies, proposed by Feldman [12], has been garnering interest as lunar exploration opportunities are expanding. This study aims to investigate the feasibility of discerning the difference of 8.6 s in the mission duration for the main mission of water exploration.

SECOND MISSION ANALYSIS

For second mission analysis, the same neutron flux simulator used in the main mission analysis was employed. Flux variations due to the presence of water were detected during the water exploration mission. Therefore, when identifying the leakage flux at the lunar surface, models with different hydrogen densities were referred. However, for lifetime measurements, varying neutron lifetimes were assumed to determine the flux dependency of neutron decay during the flight to orbit.

As shown in the top graph of Figure 11, the altitude profiles of the thermal neutron fluxes for two different neutron lifetimes, namely 879.4 s and 888.0 s, appear identical. Considering the difference between the two lifetimes, a small difference is observed at approximately 0.01% in the observed thermal neutron flux. Notably, the difference arising from the neutron lifetime does not obscure the signal indicating the presence of hydrogen during the water exploration mission.

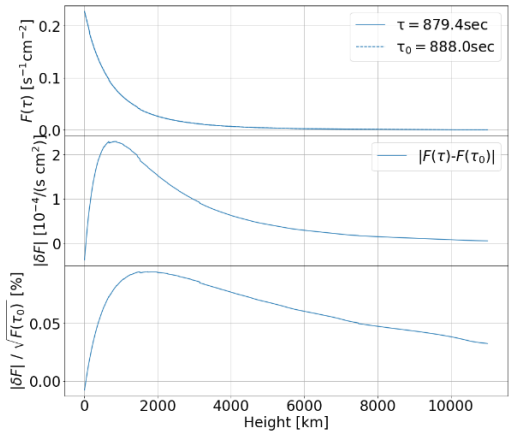

Figure 11: (Top) Altitude profile of thermal flux at two different lifetime (Middle) differential flux

between the lifetimes (Bottom) Relative differential flux intensity to statistical fluctuation

SECOND MISSION REQUIREMENTS

The second mission aimed to detect the difference in neutron flux based on an in neutron lifetime deviation of 8.6 s. To discern this difference, it is necessary to distinguish a variation of 0.397% in the observed thermal neutron counts for a statistical reliability of 3σ, derived via the time integration of flux over the estimated observation period. These requirements are listed in Table 3.

Table 3: Second mission requirement

Reqt. 3	Demonstrate the third measurement method using the ne utrons leaking from the Moon and measure the neutron l ifetime variation of 8.6 s with a statistical confidence of 3σ.

SECOND MISSION DETECTOR

The detector for the second mission was designed following a methodology similar to that used for the main mission. Two scintillator detectors were installed on the lunar side facing the satellite. First, a GS20 glass scintillator, was used for neutron detection with dimensions of 100 mm × 40 mm × 10 mm, whereas the second was a 5 mm thick EJ 270 plastic scintillator, aimed at reducing the background radiation. The latter scintillator surrounded the main detector, as shown in Figure 12, and the coincident signals for both detectors were deduced as the background flux. The MPPCs were attached to each detector. After considering the fast and epithermal neutrons, gamma rays, and other potential background sources, the background ratio k of the detector to the signal neutron flux was assumed to be 2.

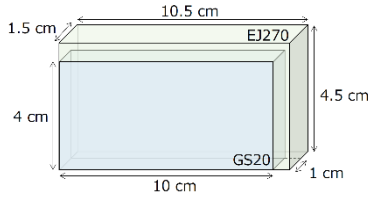

Figure 12: Scintillation detector used in the second mission for neutron lifetime measurement

To satisfy the mission requirements Table 3, the ability to detect a difference of 0.397% of the total counted thermal neutrons is required to distinguish the variation caused by the neutron lifetime gap of 8.6 s in terms of statistical error. Combining the aforementioned parameters yields a background ratio of 2, statistical reliability of 3, and a variation of 0.397%, which satisfy the following requirement: $\varepsilon S_{det}/(1+k) = 25 > 14.3$.

ORBIT DESIGN

This section describes the orbit used to accomplish the proposed mission. Additionally, it describes the orbit transfer and orbit maintenance from the separation from the launch vehicle until the end of the mission. The satellite is assumed to be aboard a transportation service such as one provided by Astrobotics and it utilizes electric propulsion as the propulsion system owing to mass constraints. The satellite performs orbit transfer from the lunar orbit to the target mission orbit, where it remains for a one-year mission period while maintaining the orbit. Because of the mass constraints, electric propulsion is typically used in propulsion systems.

Lunar frozen orbit

A frozen orbit was designed to enable a long mission duration and to pass over the South Pole at a low altitude. The elements of the designed frozen orbit were determined as follows: a = 2748 km of $\bar{a}$, 0.3602 of $\bar{e}$, 90° deg of $\bar{\imath}$, 270 deg of $\bar{\omega}$. Given the above mean orbit elements, $\bar{a}$, $\bar{e}$, $\bar{\imath}$, and $\bar{\Omega}$ can be frozen, but $\bar{\omega}$ cannot be frozen and propagates as shown in Equation (4) [13].

$$\dot{\bar{\omega}} = -\frac{3J_2\mu^{\frac{1}{2}}R_M^2}{4\bar{a}^{\frac{7}{2}}(1-\bar{e}^2)^2} - \frac{9kn_3^2\bar{a}^{\frac{3}{2}}}{4\mu^{\frac{1}{2}}\sqrt{1-\bar{e}^2}}(1-\bar{e}^2), \quad (4)$$

where J_2 = the second zonal harmonic, μ = the gravitational constant of the moon, R_M = the radius of the Moon, k = the mass ratio and n_3 = the orbital velocity of the moon. The orbit propagation results based on Equation (4) indicate that the $\bar{\omega}$ is shifted by 10° in 30 days (approximately one month) when $\bar{e}$ is 0.3602, as shown in Figure 13. To correct this shift, orbital control must be performed once every month.

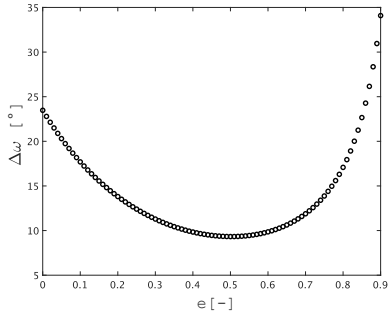

Figure 13: Extent to which $\bar{\omega}$ shifts for the selected $\bar{e}$ in the 30-day time integral.

Estimation of total ΔV

The required V for orbit control in the two-body problem with the Moon was calculated to be 100 m/s, assuming an impulsive maneuver. Furthermore, based on the paper referenced in [14], the ΔV required for station keeping

was found to be 89.9 m/s per month, due to the $\bar{\omega}$ shifting about 10° in one month. Thus, the ΔV required for a one-year mission period was calculated as $\Delta V = 100 + 89.9 \times 12 = 1178.8$ m/s.

Although this satellite employs a low-thrust propulsion system with electric propulsion, it is designed with a margin of 1.5 times because of the impulse assumption, resulting in a design value of ΔV of 1768 m/sec. However, the possibility of a small ΔV has emerged owing to the ongoing construction and verification of a detailed ΔV simulation of a low-thrust propulsion system, which requires further investigation.

Verification with high-fidelity models

In this section, in addition to the two-body problem and the perturbative forces considered in the previous sections, a more accurate model is introduced to verify the designed orbit. This model incorporates the Moon's spherical harmonic extended up to the 50th order to account for the mass concentration. It is combined with an ephemeris that encompasses the precise motion of the Sun, the Earth, and the Moon. The resulting orbit propagation in jTOP, a trajectory optimization software, is shown in Figure **14**.

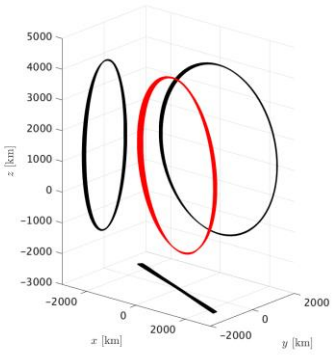

Figure 14: Orbit in high-fidelity models

POWER SYSTEM

Power requirements for each operation mode

Power requirements are calculated for each phase/mode, with a 10% margin. Table 6 summarizes the power requirements for each phase in each operation mode. Power calculations based on the Table 6 result in a maximum power requirement of 171.0 W at the end-of-life (EOL).

Solar paddle sizing

Considering the parameters in the Table 4, P(BOL), required power at the begin-of-life is obtained based on P(EOL), yielding 217.1 W.

Table 4: Parameters for solar arrays

Parameter	Value
Solar incidence angle [degree]	5
Degradation rate due to radiation	0.93
Degradation over lifetime	0.98
Degradation rate due to temperature	0.87

The HaWK38A-235 from MMA Design's HaWK series, which is a flight heritage with a deployment mechanism, is selected as a solar array to meet these requirements.

Battery sizing

Nano Power Battery 2600mAh is selected from GOM Space as the battery. Considering the parameters in the Table 5, the required battery capacity is 6.91Ah.

Table 5: Parameters for battery capacity calculation

Parameter	Value
Power consumption in the shade [W]	163
Shade time [h]	0.75
Depth of discharge	0.65
Battery cells connected in series	8
Voltage of battery cells [V]	3.6
Power transfer efficiency	0.9

A total of 28 required battery cells is used with 8 battery cells in series and 3 battery cells in parallel, due to the bus voltage being 28 V, the voltage per battery cell being 3.6 V, and the capacity being 2.6 Ah.

Power Control Equipment

The PCU-110 from Berlin Space Technologies (BST) and the PPU-200 from Space Electric Thruster Systems (SETS) are selected as power controllers. The PPU-110 meets our objectives in that it uses a PPT (Peak Power Plot) method that allows the operating point of the array to follow the maximum power, it uses a non-stabilized bus method with high power transfer efficiency, and it can convert between multiple voltages. The PPU-200 is selected because it can transform to electric propulsion voltage (200 V), which is not possible with the PCU-100.

STRUCTURE SYSTEM

The structure system is designed to meet requirements for mass and shape. The satellite structure with less than 50 kg of mass must fit into a space of 500 x 500 x 500 mm. The outer surfaces of all six sides are aluminum honeycomb panels. The propellant tank in the center is enclosed by two inner honeycomb plates, and these two panels are also used to mount equipment. The core material of the honeycomb panels is AL3/16-5052-.002 and the surface skin is made of A2024-T3.

Table 6: Power requirements for each phase / operation mode

System	equiprnent	Voltage[V]	Power[W]	INI op	orbital transfer phase			Mission Observation Phase			
					orb trans	normal	comm	obs	orb keep	comm	normal
water	DAQ(x4)	5	8					○			
	(standby)		8	○	○	○	○		○	○	○
	camera		2.6					○			
Lifetime	DAQ(x2)	5	4					○			
	(standby)		4	○	○	○	○		○	○	○
Attitude control	Star Sensors	5.2-5.4	1.2	○	○	○	○	○	○	○	○
	Gyro Sensors	3.3	0.016	○	○	○	○	○	○	○	○
	Sun Sensor	3.3/5	0.04	○	○	○	○	○	○	○	○
	RW	28	6.6	○	○	○	○	○	○	○	○
			10.5		○				○		
	thruster(CGT)	28									
	(Standby)		1.3	○		○	○	○		○	○
Thermal Control	heater	28	5	○		○	○	○		○	○
Power	Power Control Unit	28	4	○	○	○	○	○	○	○	○
Communication	transponder(RARR)	28	7.9	○	○	○		○	○		○
	(Mission / HK)		23.6				○			○	
C&DH	CPU		5	○	○	○	○	○	○	○	○
propulsion	electric propulsion	200	115		○				○		
Total power requirement[W]				43.0	151.7	43.0	58.7	45.6	151.7	58.7	43.0
10%surplus [W]				47.3	166.9	47.3	64.6	50.1	166.9	64.6	47.3

The origin of the coordinates of the satellite is set in the center of the bottom face of the rocket interface. The X-axis is directed toward the solar panel mounting surface, the Z-axis toward the direction of the neutron telescope, and the Y-axis is set following right-hand system. Table 7 shows the center of gravity and inertial moment of the satellite before and after solar array panel deployment. Also, Table 8 shows mass budgets of the satellite with items of each subsystem.

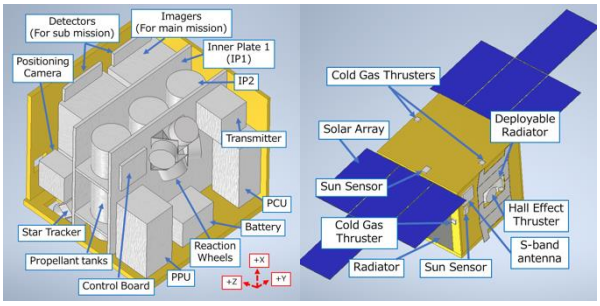

Figure 15: Internal and external view of the proposed satellite structure

Table 7：Mass Properties

Margin		Before deployment	After deployment
Center of Gravity [mm]	x	267	278
	y	0.592	0.592
	z	-3.17	-3.17
Inertial Moment [kgm^2]	xx	1.56	2.26
	xy	0.00923	0.00951
	xz	0.0130	0.0114
	yy	1.30	1.42
	yz	-0.0786	-0.0786
	zz	1.42	2.16

Table 8: Mass Budgets

System	Est. Mass [kg]	Items
Main Msn.	11.9	Detector, Telescope structure, Circuit boards, positioning camera
Sec. Msn.	0.4	Detector, Structure, Circuit boards
Power	5.5	Solar cell, PCU, PPU, Battery
Comm. & TT&C	1.4	S-band transmitter, S-band antenna, MCU
Propulsion	15.2	BHT-100, Propellant Tanks, CGT
Thermal	0.6	Heater, Reversible thermal panerl
ADC & Navigation	1.2	Star tracker, Gyro sensor, Sun sensors, RW, Control board
Structure	6.2	Honeycomb plates, Rocket Interface, Harness & wire
Margin	7.6	System margin about 15%
Total	50.0	

A structural analysis in Autodesk Inventor is performed using the simplified model to confirm whether the satellite structure meets the requirements for an assumed launch environment on H2A. After the following four analysis, strength analysis, natural frequency analysis, sinusoidal vibration analysis and random vibration analysis, the results show that satellite withstands the

mechanical environment during launch with positive margin of safety in all cases. In the worst case, stress on inner honeycomb plate becomes the largest, where the margin of safety records smallest as 0.39.

THERMAL CONTROL SYSTEM

The requirements for the thermal control system are that the temperature of the onboard equipment is always within the allowable temperature range. The satellite is in an elliptical orbit with a perilune distance of 20 km and apolune distance of 2000 km, and the sun inclination angle is $\beta = 0° \sim 90°$. Thermal control is operated independently in the following three sub system; satellite structure, thruster, and solar array panels.

For satellite structure, generated heat from inner components is dissipated to ±Y surface, where OSRs are used for radiators. Other surfaces except for radiators including +X surface are insulated. The inner sides of each panel are painted black to foster internal heat exchanges.

To maintain a thermal condition of hall effect thruster with a peak heat generation of 54 W, a reversible thermal panel (RTP) is introduced [15]. RTP is attached with shape memory alloys on its movable parts, and it opens and closes passively in response to temperature. The area of radiation is 0.016 m^2 when the thruster is not working and 0.10 m^2 when working.

Heat input from the surface of the solar panel is dissipated directly from the back surface. To reduce the heat input, BRR (Blue and Red Reflective) coating is applied on the solar panels [16]. Z-93 coating is applied on the back surface because of its low absorption and high emissivity.

Analysis result

A thermal mathematical model is constructed with Thermal Desktop and solved by SINDA/FLUINT. Figure 16 shows the result of thermal analysis by Thermal Desktop when $\beta = 90°$ and thruster is operating. Figure 17 shows the allowable temperature range and operating temperature range of each device. Temperatures of all equipment are confirmed to be in the allowable range.

ATTITUDE CONTROL SYSTEM

Attitude Stabilization

The mission requires that the attitude of the satellite remain stationary while telescopes point toward the lunar surface. To achieve high-resolution observations is 0.1 deg, this satellite adopts the 3-axis zero-momentum stabilization as its attitude stabilization.

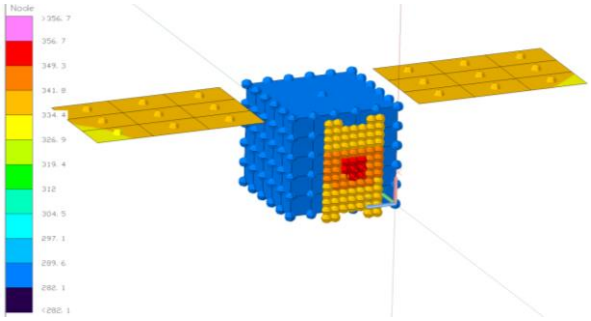

Figure 16: Result of thermal analysis

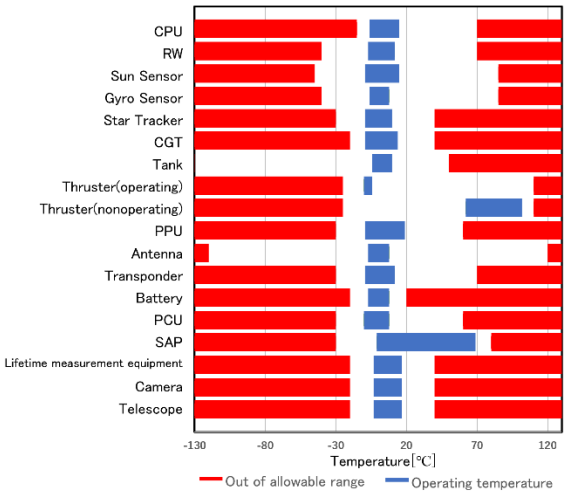

Figure 17: Allowable temperature range and operating temperature range of each device

Attitude Determination

This satellite equips a star tracker, four sun sensors, and an inertial measurement unit (IMU), and ST-1 from NanoAvionics, SSOC-A60 from Solar MEMS, and M-G370 from Epson is selected respectively. To manage data with errors from sensors, Multiplicative Quaternion Extended Kalman Filter (MEKF) is used for error correction.

Attitude Control

The actuator is reaction wheel (RW), which does not utilize propellant and has been used on many small satellites, and RW-0.06 from Rocket Lab is selected. The saturated angular momentum of each RW is 0.18 Nms. To provide redundancy, four RWs are installed and arranged in a pyramid configuration (4-skew arrangement). The skew angle is 35.26 deg.

The attitude of the satellite is expressed by Euler parameters. Since this mission requires the satellite to be stationary, rest-to-rest attitude change is considered. The

equation of motion of the satellite with RWs in the fixed coordinate system is expressed as follows.

$$\dot{\boldsymbol{H}}_{\mathrm{B}} + \boldsymbol{\omega}_{\mathrm{B}} \times \boldsymbol{H}_{\mathrm{B}} = \boldsymbol{T}_{\mathrm{out}} \quad (5)$$

where $\boldsymbol{H}_{\mathrm{B}}$ = angular momentum, $\boldsymbol{\omega}_{\mathrm{B}}$ = angular rate of the satellite, and $\boldsymbol{T}_{\mathrm{out}}$ = disturbance torque.

Given $\boldsymbol{T}_{\mathrm{out}} = 0$, the required torque for attitude change $\boldsymbol{\tau}$ is obtained by quaternion feedback as follows.

$$\boldsymbol{\tau} = k_{\mathrm{p}}\bar{\boldsymbol{q}}_{\mathrm{e}} - k_{\mathrm{d}}\boldsymbol{\omega}_{\mathrm{B}} \quad (6)$$

where k_{p} = proportional gain, $\bar{\boldsymbol{q}}_{\mathrm{e}}$ = vector part of the error quaternion, and k_{d} = differential gain.

The control input, angular momentum $\boldsymbol{h}_{\mathrm{RW}}$, is obtained by the following equation so that the required torque is generated with each angular momentum of RWs to be the nominal value, $\boldsymbol{h}_0$, at the end of the attitude change.

$$\boldsymbol{u} = \boldsymbol{W}^{\dagger}(-\boldsymbol{\tau} - \boldsymbol{\omega}_{\mathrm{B}} \times \boldsymbol{h}_{\mathrm{RW}}) - k_h(\boldsymbol{h}_{\mathrm{RW}} - \boldsymbol{h}_0) \quad (7)$$

where $\boldsymbol{W}^{\dagger}$ = pseudo-inverse of the wheel spin direction matrix, k_{h} = weighting factor.

The worst case for attitude changes in observation mode is when the satellite rotates 180 degrees. simulation results for this case are shown in Figure 18. Even in this worst case, the satellite can reach the target attitude and stabilize within about one minute.

Disturbance Torque

Since this satellite orbits the Moon, only solar radiation pressure torque and gravity gradient torque are considered. The angular momentum accumulated by disturbance torque during the mission period (one year) of this satellite is 13.0 Nms. If half of the saturated angular momentum accumulates in any one of the four RWs, unloading (UL) is performed using cold gas thrusters (CGT) as soon as possible.

PROPULSION SYSTEM

Thruster Select

The propulsion system plays the following three roles; (A) orbit transferring, (B) orbit maintenance in the frozen orbit, and (C) unloading (UL). The ΔV required from orbit simulation for (A, B) is 1768 m /s. To achieve this with chemical propulsion about 20.58 kg of propellant is required. However, this is difficult to achieve, so electric propulsion should be used. In addition, to achieve the required ΔV while keeping the injection time to less than half of the mission duration, a thrust of at least 5 mN is necessary. The power required for the propulsion system of this satellite is about 100 W.

Therefore, a thrust power ratio of about 50 mN/kW is required. The Hall thruster (HET) BHT-100 from Busek is selected as the propulsion system that satisfies these requirements. Xenon is selected as a propellant due to thruster response, allowable temperature, ease of ground testing, and technology maturity.

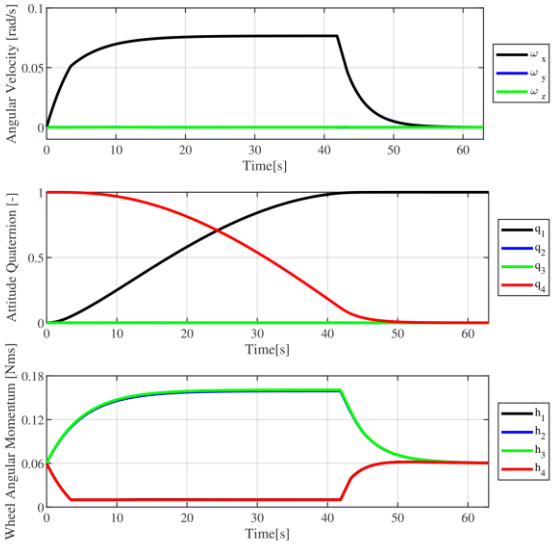

Figure 18: Satellite Angular Velocity (top), Satellite Attitude (middle), and Angular Momentum of RWs (bottom) during the Worst Case of Attitude Change

Next, a cold gas jet thruster (CGT) is adopted for (C), assuming that the xenon propellant is shared with the HET. Although the specific impulse for CGT is small, it can be realized with a relatively simple structure. Eight xenon CGTs 58E163A from Moog are installed. The amount of propellant required for (C) is calculated to be 234 g to satisfy requirement form ADC operation. エラー！参照元が見つかりません。 summarizes the designed parameters for each thruster based on the previous section.

Table 9: Parameters for Thrusters

Parameter	HET (BHT-100)	CGT (58E163A)
Propellant	Xenon	Xenon
Thrust	7.25 mN	1.3 N
Specific impulse	1067 s	21 s
Discharge Voltage	200 V	-
Discharge Current	0.51 A	-
Total Power	115 W	-
Response	-	0.01 s

Tank Design and System Configuration

The tank specifications are shown in Table 10. The tank stores xenon, the common propellant for HET and CGT, in a supercritical state. The maximum expected operating pressure (MEOP) in the tank is set to be less than 10 MPa. The required xenon mass is 8.00 kg plus a margin of 9.00 kg, and the tank volume is first determined so that the pressure does not exceed 10 MPa at the upper limit of the tank temperature, 50 °C, where the pressure is greatest. The total length of the tank is set to be within 370 mm due to structural limitations.

Table 10: Parameters for Tanks

Parameter	Value
Material	Ti-6Al-4V
Overall Length	362.4 mm
Thickness	1.2 mm
Quantity	3
Total Volume	9220 cm^3

Finally, the configuration of the propulsion system is shown in Figure 19.

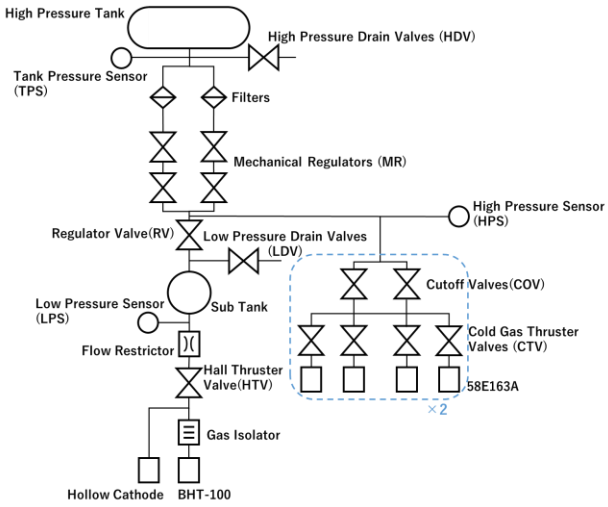

Figure 19: Propulsion System Configuration

COMMAND AND DATA HANDLING

A flight heritage board, the SatBus 3C2 OBC from NanoAvionics, is selected to process and store HK data and mission data acquired from each bus system, as well as command data received from ground stations. The acquired data is stored on a microSD (32 GB) in the OBC.

Next, the amount of communication data is considered that is transmitted and received between the satellite and the ground station. Estimated data amounts for three types of data are 400 bits of command data, 560 bits of HK data, and 346,667 bits of mission data.

COMUNICATION SYSTEM

Communications equipment

The satellite utilizes an S-band transponder from L3HARRIS for both uplink and downlink. The satellite is equipped with two ANYWAVES S-band antennas mounted on opposite sides of the satellite, enabling communication with the ground station regardless of its attitude. Usuda Deep Space Center (UDSC) serves as the ground station, facilitating TT&C communications via the S-band.

Analysis of communication available time

Communication availability time is evaluated through simulations conducted using the System Tool Kit (STK). The results indicate that the required communication time of approximately 20.1 minutes for receiving command data and transmitting HK and mission data is within the available time.

Circuit design

Circuit design for uplink and downlink lines considers the onboard antenna's gain condition at its lowest value. Line margins for uplink and downlink are designed to satisfy power flux density (PFD) requirements and maintain minimum values of 10 dB and 1 dB, respectively. The obtained uplink and downlink line margins are adequate, and PFD requirements conform to the specified value.

POSITIONING AND ORBIT DETERMINATION

Range And Range Rate (RARR) method is used for orbit determination. Downlink/uplink frequency ratio is set to 240/221 to adopt the coherent demodulation based on [17]. When the ground station is visible from the satellite, communication for RARR is always conducted. According to [18], the angular accuracy in orbit determination operations using RARR data is about 1 μ rad. When considering this for position determination accuracy on the Moon's orbit at approximately 300,000 km from Earth, the orbit determination accuracy is estimated to be around 3 km.

Optical Camera-based Error Correction

The primary objective of this mission is to create a neutron map with a 5 km resolution. However, as mentioned earlier, there remains an error of about 3 km in orbit determination using radio waves. This error of approximately 3 km is an unacceptable magnitude for a 5 km resolution.

A optical camera named Gecko with a spatial resolution of 39 m is selected. During the closest approach to the Moon, images are captured simultaneously with neutron

observation, and transmitted to the ground. Subsequently, by matching with Kaguya's 10 m resolution optical map, the error in the observation range of the neutron map obtained using orbit determination is corrected. The observation range can be determined with an accuracy of several tens of meters by the optical camera. As a result, the error in the observation range is sufficiently reduced for the 5 km resolution.

CONCLUSION

The proposed satellite named as "Izumi" explores lunar water resources, which is a key to future deep space exploration beyond the Moon. High-resolution neutron survey has not been achieved despite its importance of subsurface evaluation in the utilization of water resources. The satellite utilizes a thermal neutron imager to overcome the bottleneck of previous missions and achieve a 5 km resolution mapping that can be used in practical applications. We hope that "Izumi" provides a foundation for the development of new lunar industries such as resource utilization and base construction, as well as deep space exploration to Mars.

ACKNOWLEDGEMENT

This proposal is supported by other students and faculty members. As the "Izumi" student team, we would like to thank Raiki Kudo (The University of Tokyo), Azumi Izawa (Aoyama Gakuin University), So Kaieda (Yokohama National University), Naoto Aizawa (The University of Tokyo), Yutaro Nagai (Kyoto University). Also, we would like to express our sincere gratitude to Teruaki Enoto (RIKEN / Kyoto University), Hiroshi Nagaoka (RIKEN), Naoki Tsuji (Kyoto University), Yoshie Otake (RIKEN), Takaoki Takanashi (RIKEN), Masaki Numazawa (Tokyo Metropolitan University), Makoto Hareyama (St. Marianna University), Hiroki Kusano (QST), Takashi Okajima (NASA GSFC) for their invaluable assistance in the development of the science mission.

REFERENCE

1. Haruyama, J., et al., "Lack of Exposed Ice Inside Lunar South Pole Shackleton Crater," Science, 322, 5903, 938-939, 2008.
2. Lawrence et al., "Performance of Orbital Neutron Instruments for Spatially Resolved Hydrogen Measurements of Airless Planetary Bodies," Astrobiology, 183-200, 2010.
3. H.M. Brown, et al., "Resource potential of lunar permanently shadowed regions," Icarus, Volume 377, 2022.
4. Mitrofanov, I.G., et al. "Lunar Exploration Neutron Detector for the NASA Lunar Reconnaissance Orbiter," Space Sci Rev 150, 183–207, 2010.
5. C. Hardgrove, et al., "The Lunar Polar Hydrogen Mapper CubeSat Mission," IEEE Aerospace and Electronic Systems Magazine, March 2020.
6. Kusano et al., in preparation
7. Feldman, W. C., et al., "Gravitational effects on planetary neutron flux spectra," J. Geophys. Res., 94(B1), 513– 525, 1989.
8. Stopar J. et al., "Topographic Map of the Moon's South Pole (80°S to Pole)", LPI-RPIF, LPI Contribution 2169, 2019
9. T. Hosobata et al., "Elliptic neutron-focusing supermirror for illuminating small samples in neutron reflectometry," Opt. Express 27, 26807-26820 2019
10. Y. Ezoe et al., "Ultralightweight x-ray telescope missions: ORBIS and GEO-X," J. Astron. Telesc. Instrum. Syst. 4(4) 046001 4 October 2018
11. Wietfeldt, F.E., et al., "Measurements of the Neutron Lifetime." Atoms, 6(4):70, 2018.
12. W.C. Feldman, et al., "A technique to measure the neutron lifetime from low-earth orbit," Nucl. Instrum. Methods Phys. Res., 1990.
13. Sandeep Kumar Singh. et al., "Feasibility of quasi-frozen, near-polar and extremely low-altitude lunar orbits," Acta Astronautica, 2020.
14. Theodore Sweetser, "How to Maneuver Around in Eccentricity Vector Space," AIAA/AAS Astrodynamics Specialist Conference, August 2010
15. Nagano, H. et al, "Study on thermal radiation and retention control for spacecrafts using a re-deployable radiator," Proceedings of Thermal Engineering Conference, Tokyo, November 2006.
16. Beauchamp, W.T., et al., "Qualification test results for blue-red reflecting solar cell covers and other new products for the solar power market," Proceedings of 1994 IEEE 1st WCPEC, 1994.
17. JAXA. RF Communication System Design Standard. 2019. Retrieved: 2023/04/12
18. Yoshihiko Asai, et al., "Highly Accurate Orbit Determination Using Differential VLBI Technique", Transactions of the Society of Instrument and Control Engineers, Vol. 35, No. 4, p. 467-472, 1999